

# Miniaturized mmWave Tri-Band VCO Using Self- and Mutual-Mode-Controlled Inductor

Seongwoog Oh<sup>1b</sup>, Graduate Student Member, IEEE, and Jungsuek Oh<sup>1b</sup>, Senior Member, IEEE

**Abstract**—This article presents a miniaturized tri-band complementary metal-oxide-semiconductor (CMOS) voltage-controlled oscillator (VCO) utilizing the self- and mutual-mode-controlled inductor (SMCI) without increasing chip area. Additionally, the degradation in phase noise due to the ON-resistance of the switch used for reconfigurable operation is eliminated with a configuration of paired switches and multiple oscillation cores. The proposed SMCI includes outer and inner windings with a center winding connected to the middle of the other two windings; it operates in three modes resulting in different inductances by reconfiguring the connectivity of the four ports. Graphical optimization based on the equivalent circuit with a mutual analysis of segment modeled SMCI is used to present a design strategy in which the inductance of each mode can be independently adjusted in terms of the target frequency ratio. The VCO implemented in a 28-nm CMOS process exhibits a frequency ranging from 16.79–20, 21.87–25.8, and 32.01–38.3 GHz for each band with the corresponding phase noise and tuning range figure-of-merit (FoM<sub>T</sub>) values of –189, –188.3, and –187.8 dBc/Hz. The fabricated chip consumes average power of 12.73 mW and occupies an area of 0.043 mm<sup>2</sup>.

**Index Terms**—Inductive frequency tuning, inductor, millimeter wave (mmWave) circuits, multimode inductor, tri-band, voltage-controlled oscillator (VCO).

## I. INTRODUCTION

THE millimeter-wave (mmWave) band has potential applications in high-speed data transmission owing to its wide bandwidth [1], [2]; to this end, a considerable amount of research and commercialization are currently in progress in the field of communication [3], [4], [5]. Among these efforts, an extensive amount of research has focused on several components at the system level for mmWave frequency bands of the fifth-generation (5G) mobile and satellite communication [6], [7]. A component or system that can support these

Manuscript received 25 October 2022; revised 12 January 2023 and 23 February 2023; accepted 17 March 2023. Date of publication 11 April 2023; date of current version 5 October 2023. This work was supported in part by the Institute of Information and Communications Technology Planning and Evaluation (IITP) grant funded by the Korean Government (MSIT) (Millimeter-wave Metasurface-based Dual-band Beamforming Antenna-on-Package Technology for 5G Smartphone) under Grant 2020-0-00858 and in part by Samsung Electronics (Development of Dualband/Wide-band High Efficiency Power Amplifier MMIC for 5G Applications). This article is an expanded version from the 2021 IEEE RFIC Symposium [DOI: 10.1109/RFIC51843.2021.9490477]. (Corresponding author: Jungsuek Oh.)

The authors are with the Department of Electrical and Computer Engineering (ECE), Institute of New Media and Communications (INMC), Seoul National University, Seoul 151-742, South Korea (e-mail: jungsuek@snu.ac.kr).

Color versions of one or more figures in this article are available at <https://doi.org/10.1109/TMTT.2023.3263590>.

Digital Object Identifier 10.1109/TMTT.2023.3263590

0018-9480 © 2023 IEEE. Personal use is permitted, but republication/redistribution requires IEEE permission. See <https://www.ieee.org/publications/rights/index.html> for more information.

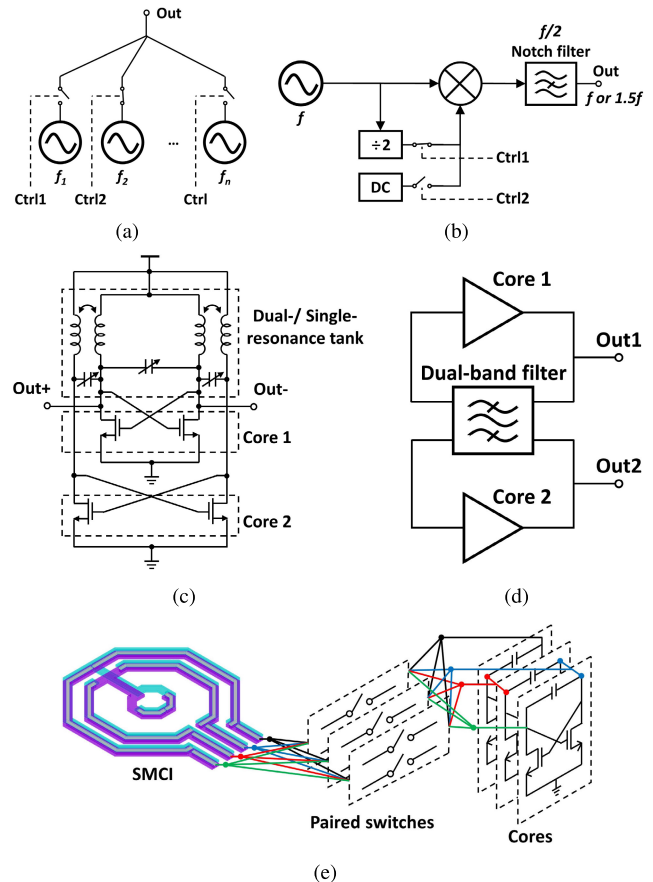


Fig. 1. Conventional multiband VCOs with different topologies of (a) multiple single-band optimized VCOs, (b) mixer-based dual-band VCO, (c) transformer–varactor coupled tri-band VCO, and (d) filter-based dual-band VCO. (e) Conceptual diagram of the proposed tri-band VCO using MCSMI.

mmWave applications must ensure multiband operation within the allocated frequency spectrum at the  $K$ - and  $Ka$ -bands. Accordingly, it is assumed that a voltage-controlled oscillator (VCO)—an essential circuit commonly used for transmission or reception in a transceiver system—requires multiband support [8], [9]. However, the size of the integrated circuit system increases when VCOs suitable for each band are used individually because the VCO consists of inductor components that consume a large chip area; this also results in high costs. Thus, there is a need to develop a miniaturized multiband VCO as a signal source for multiband communication systems [10].

Diversified dual- and tri-band studies have focused on the development of multiband VCOs. Fig. 1(a) shows the topology in which each VCO is optimized for a different single band and combined through a switch configuration [11].

This configuration has an advantage in that the VCO has the most optimized performance in each band; however, the issue related to a large chip area still exists because of the primitive extension method. In particular, three and six switch circuits are required to implement the tri-band characteristics of single-ended and differential signals, respectively. Further, parasitic components generated by the switch and the impedance mismatch caused by multiple switches degrade the performance. Also, the relationship between limited RF performance by the number of switches linearly increasing in the number of bands, should be resolved. As indicated in Fig. 1(b), a mixer-utilized architecture is adopted for isolating the effects of the parasitic component of the switch from the VCO output signal path when switching the oscillation frequency band [12]. The scheme wherein a divider, mixer, and notch filter are added for dual-band implementation has high complexity and limited frequency multiplication between bands. For example, if band switching occurs via dc and the divider of factor 2, the frequency ratio between the bands is limited to 1.5 and the ratio value is discrete even after adjusting the dividing factor. The inductive component in the notch filter is used to remove unintended frequencies from the mixer output and consumes a large portion of chips. Fig. 1(c) shows a schematic of a tri-band VCO with a transformer and varactor to construct a dual- and single-resonant tank [13]. Inductive and capacitive couplings are simultaneously generated through the transformer and the varactor to form multiple resonances; this provides the advantage of enabling tri-band oscillation with a relatively simple active-device configuration. The phase noise performance of the VCO is low because of the low  $Q$ -factor when the resonant tank is implemented as a transformer and coupled varactor [14]. Further, the parasitic capacitances of varactors and transformers connected to the oscillating core severely limit the frequency tuning range (FTR). As shown in Fig. 1(d), two cores and a dual-band bandpass filter are combined to separate the oscillated signals for two bands at each port [15]. A balun structure that combines the two VCO outputs into a single port must be designed when combined with a transceiver operating in multiple bands. Several inductive elements must be arranged to generate coupling to implement dual-band characteristics or higher in the filter, which can consume a large chip area. Furthermore, the technique of laying out with multiple turns to reduce the area occupied by the inductor structure is difficult to be widely used due to a limitation of the self-resonance frequency at mmWaves [16]. Therefore, most studies use an inductor of one turn or up to two turns as a resonator.

Based on prior studies, the challenges that a tri-band VCO must overcome can be classified into a minimized chip area, minimization of switch effects for reconfigured operation, and a high degree of freedom in band selection. The number of inductive components that require the most significant VCO chip area should be minimized. As switches increase in size, their ON-resistance and OFF-capacitance decreases and increases, respectively, and this minimizes the simultaneous effect on the phase noise and FTR. The degree of freedom to ensure optimized design for any frequency band ratio is very important since frequency bands used for 5G and satellite

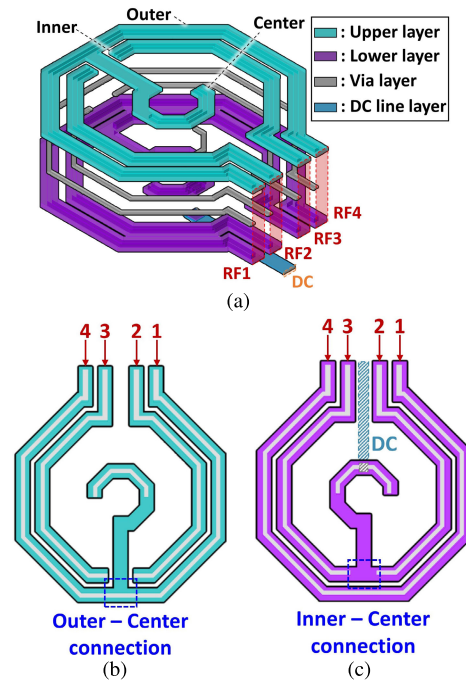


Fig. 2. (a) Exploded, (b) upper layer, and (c) lower layer with dc path view of the proposed SMCI.

communication are widely distributed across the  $K$ - and  $Ka$ -bands. As a solution to these challenges, a miniaturized tri-band VCO with high freedom in designing frequency bands is proposed in this article; this is illustrated in Fig. 1(e) with a self- and mutual-mode-controlled inductor (SMCI) with a novel reconfigurable mechanism, paired switches, and three cores.

The remainder of this article is organized as follows. Section II introduces the miniaturized SMCI architecture and an optimization method based on the inductance and  $Q$ -factor analysis. Section III presents the structure of a triple-core in VCO using SMCI through a paired switch configuration and the resonant frequency analysis is conducted. In Section IV, the fabricated circuit and measurement results are presented, and the conclusions are provided.

## II. CONCEPT AND ANALYSIS

The proposed SMCI comprises outer, inner, and center windings, as shown in Fig. 2(a). The outer and inner windings use upper and lower metal layers connected with vias to minimize the  $Q$ -factor reduction caused by metal resistance. The center winding has only three-quarters of the upper and lower metal layers with half overlapped via layer as shown in Fig. 2(b) and (c) to prevent short-circuiting both nodes. Each node of the center winding is connected to the center of the outer and inner windings. Further, considering the utilization with the VCO, a dc path for biasing is connected to the middle of the center winding to minimize the influence on the mmWave characteristics. The SMCI structure has three separate windings with four ports through which RF signals are excited because both nodes of the center winding are connected to the other winding.

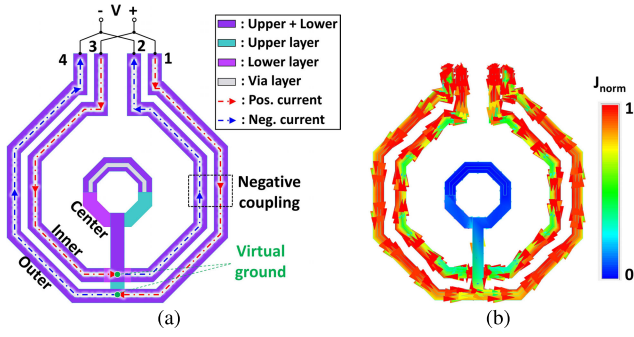


Fig. 3. (a) Excited current paths diagram and (b) simulated current distribution of the odd-mode operation.

### A. Current-Based Multimode Excitation

The mode operation of SMCI is achieved by the polarity of the potential excited to each RF port. The effect of the dc path is neglected in the analysis of the RF current because it is located at the virtual ground node and connected to the ground through a sufficiently large capacitance. As shown in Fig. 3(a), when ports 1 and 3 are positive while ports 2 and 4 are negatively excited, the current flowing along each outer and inner winding becomes opposite, which is called the odd mode. There is no current flowing into the center winding in the odd mode because both ends of the center winding are connected to the center tap where the virtual ground forms on the outer and inner windings, respectively. Virtual ground is always formed at the center tap regardless of the gap between the two windings because the outer and inner windings always operate in a differential mode. There is negligible current flowing along the center winding because of the same potential formed across both ends, which is confirmed through the simulated current distribution diagram in Fig. 3(b). Therefore, it is necessary to consider only the effect of mutual interference between the currents flowing along the outer and inner windings. Considering the two most tightly coupled currents and neglecting other mutual effects, the effective mutual inductance generated by the coupling is negative. The simplified equivalent circuit of the odd mode can be represented as a coupled circuit by connecting two inductors with the outer and inner self-inductances in parallel.  $L_o$  and  $L_i$  represent the self-inductances of the outer and inner windings, respectively, and  $M_{oi}$  denotes the effective mutual inductance between the outer and inner windings. The odd-mode inductance  $L_{\text{odd}}$ , obtained through the equivalent circuit, is

$$L_{\text{odd}} = \frac{L_o L_i - M_{oi}^2}{L_o + L_i + 2 M_{oi}} \quad (1)$$

where  $M_{oi}$  is positive because the negative coupling caused by the opposite current direction has already been reflected in the derived equation.

The even mode is a case where the current directions of the outer and inner windings coincide when ports 1 and 2 are positively excited and ports 3 and 4 are negatively excited, as shown in Fig. 4(a). The even mode generates virtual ground at both ends of the center winding like in the odd mode, which results in negligible current through the center

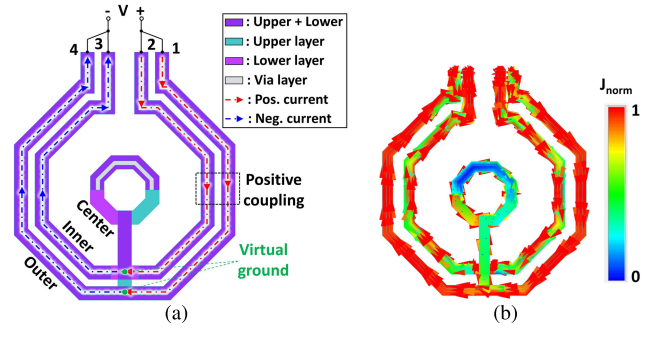


Fig. 4. (a) Excited current paths diagram and (b) simulated current distribution of the even-mode operation.

winding; therefore, only the outer and inner windings are considered when composing an equivalent circuit. As can be seen from the distribution diagram in Fig. 4(b), the current flowing to the center winding is relatively large compared to the odd mode. The couplings generated in the feed line for the connection between the center winding and other two windings are added because the currents of the outer and inner windings have the same direction. The center winding effect is omitted from the analysis because the current flowing in the center winding is sufficiently small to be negligible. The simplified even-mode equivalent circuit is driven considering that the effective mutual coupling between the two windings is positive. The even-mode inductance  $L_{\text{even}}$  obtained through the equivalent circuit is

$$L_{\text{even}} = \frac{L_o L_i - M_{oi}^2}{L_o + L_i - 2 M_{oi}}. \quad (2)$$

Compared with the odd-mode inductance (1), it can be seen that the even-mode inductance is always greater because of the positive coupling effect located in the denominator. Further, the difference between the inductances of the two modes can be designed by adjusting the mutual coupling.

The current distribution is shown in Fig. 5(a), when ports 1 and 4 are positively excited and ports 2 and 3 are negatively excited, called the expansion mode. In the expansion mode, unlike the previous two modes, the outer and inner windings no longer operate in the differential mode. Thus, a potential other than virtual ground is formed at the center taps of the outer and inner windings, which causes the current to flow into the center winding. The current direction starts at ports 1 and 4 and flows through the outer, central, and inner windings in that order, terminating at ports 2 and 3, as shown in Fig. 5(b). Therefore, a dc line must be connected to the center tap of the center winding for dc bias with negligible RF influence on even and odd modes. In odd and even modes, a differential signal is excited to the ports of the inner winding, which cancels the induced current on the dc line. Unlike the previous two modes, the expansion mode excites signals of the same phase to the two ports in the inner winding. So, a net current is induced to the dc line, creating an additional negative mutual. The dc line is still not a significant factor as it shows an inductance change of only 3%. The coupling between the currents in the expansion mode can be divided into three parts. First, the interaction

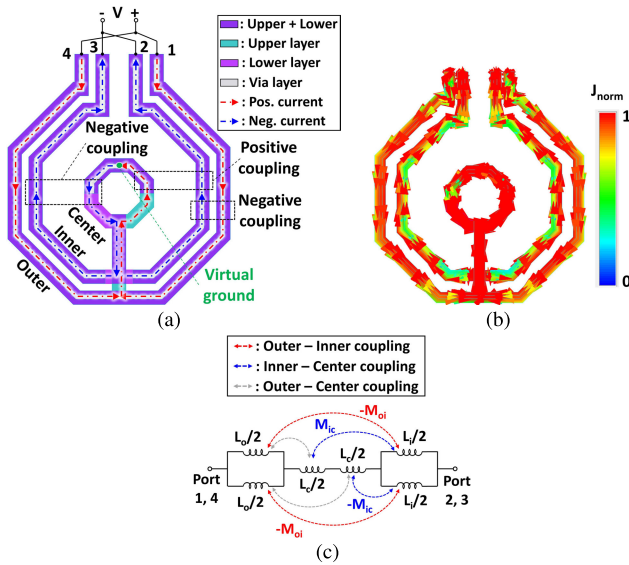


Fig. 5. (a) Excited current paths diagram, (b) simulated current distribution, and (c) simplified equivalent circuit of the expansion-mode operation.

between the outer and inner windings, which was the most important in the previous two modes. As indicated from the current distribution diagram, the mutual inductance caused by the coupling between the two windings is always negative. Second, the mutual inductance caused by the coupling between the inner and center windings. In this case, for the proposed SMCI region, the mutual inductances of the inner and center windings are positive for the right half and negative for the other left half. Third, the coupling effect between the outer and center windings. This has the opposite sign to the mutual inductance of the inner and center windings for the same region of the SMCI. The mutual coupling between the outer and center windings is negligible compared to the other two adjacent windings, given that the inner windings located in the middle interfere and couple over relatively long distances. An equivalent circuit that reflects the relationship between the inductor representing each winding, and the mutual inductance of each winding based on the current distribution is shown in Fig. 5(c).  $L_c$  denotes the self-inductance of the center winding, and  $M_{ic}$  denotes the mutual inductance between the inner and center windings. The expansion-mode inductance  $L_{exp}$ , obtained through the equivalent circuit is expressed as

$$L_{exp} = \frac{L_o + L_i}{4} + L_c - M_{oi} - \frac{4L_i M_{ic}}{L_o L_i - 4M_{oi}^2}. \quad (3)$$

Simulations were performed using an electromagnetic (EM) analysis tool to verify the effects of self-inductance and mutual inductance through the equations derived from each mode. Fig. 6(a) shows the results of the normalized inductance and  $Q$ -factor of the odd and even modes obtained when the gap between the inner and outer windings is varied while maintaining the width and average diameter of the two windings at 25 GHz. A gap from 0 to near 2  $\mu\text{m}$  indicates a region difficult to use practically because it violates the design rule check (DRC) of the semiconductor process. As the gap increases, the inductance ratio between the odd and even modes,  $L_{even}/L_{odd}$ , decreases from 7.56 to 2.33. An average

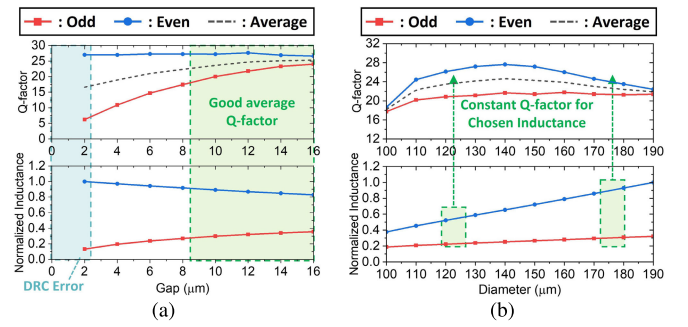


Fig. 6. Simulated normalized inductance and  $Q$ -factor with (a) variation of outer-inner winding gap, and (b) average diameter.

TABLE I  
GEOMETRIC PARAMETERS OF PROPOSED STRUCTURE

Parameter	Description
$D_c$	Diameter of center winding
$D_{in}$	Diameter of inner winding
$D_{out}$	Diameter of outer winding
$W_c$	Width of center winding
$W_{in}$	Width of inner winding
$W_{out}$	Width of outer winding
$T$	Thickness of winding metal

$Q$ -factor is introduced as a parameter to consider the  $Q$ -factor ratio between the two modes in the plot. If the outer and inner windings are too close, negative coupling between the two windings in the odd mode will result in a low  $Q$ -factor, which makes them difficult to use in VCOs. For the 8.5- $\mu\text{m}$  gap that corresponds to the average  $Q$ -factor value equal to 24.6, the normalized inductance and  $Q$ -factor values according to the average diameter of the outer and inner windings can be seen in Fig. 6(b). The coupling coefficient is constant owing to the constant gap, and the relative  $Q$ -factor value is flat at approximately 24.6 as the average diameter changes. Meanwhile, when the diameter changes from 100 to 190  $\mu\text{m}$ , the odd- and even-mode inductance ratios can be freely changed from 2.01 to 3.11. A further increase in the inductance ratio can be achieved for diameters greater than 200  $\mu\text{m}$ . However, the reduced self-resonant frequency attributed to the larger parasitic may limit its use in mmWave band applications [17].

### B. Geometric Parameter Analysis

Extended equations that reflect geometric parameters for the inductances from Section II-A are derived to provide detailed insight into the design of the proposed SMCI. The geometric parameters of SMCI are listed in Table I. Each winding of SMCI has an octagonal configuration and can be divided into segments for analysis. The equivalent circuit for each segment can be simplified into series of inductor and resistor with parallel capacitors [18].

Single-loop structural properties neglect the series parasitic capacitance used in the inductor segmented model; the parallel resistance and capacitance induced by the substrate are eliminated by the patterned ground shield, which is widely used in inductor design.  $L_s$  and  $R_s$  represent the self-inductance

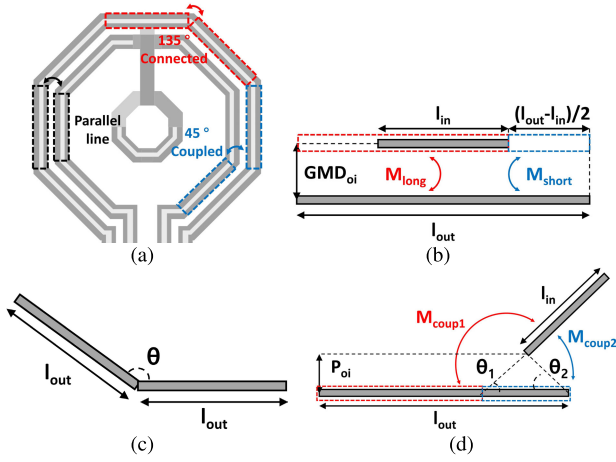


Fig. 7. (a) Diagram of dominant mutual inductance relationship occurring in the proposed SMCI. Two segments of (b) different lengths and positioned parallel, (c) equal length and connected angled ends, and (d) different lengths with a coupling angled apart.

and resistance of the segment, respectively, and  $C_{ox}$  denotes the parasitic capacitance attributed to the oxide layer. Each component can be formulated using geometric parameters as [19], [20], [21], [22]

$$L_s = 2l \left[ \ln \left( \frac{2l}{W+T} \right) + 0.50049 + \frac{W+T}{3l} \right] \quad (4)$$

$$R_s = k \frac{\rho l}{W\delta(1 - e^{-T/\delta})} \quad (5)$$

$$C_{ox} = \frac{1}{2} l W \frac{\epsilon_{ox}}{T_{ox}} \quad (6)$$

where

$$l = \frac{D}{1 + \sqrt{2}}. \quad (7)$$

$D$  and  $W$  represent the diameter and linewidth of the winding corresponding to the segment, respectively. Additionally,  $k$ ,  $\rho$ ,  $\delta$ , and  $T$  denote the fitting coefficient, resistivity, skin depth, and metal layer thickness, respectively. The relationship between  $D$  and the segment length  $l$  in (7), holds only for the single-loop octagonal inductor.

It is essential to consider the mutual inductance caused by the coupling between the inductors formed by each segment to analyze the proposed SMCI. The case of mutual inductance that can occur in the proposed structure is analyzed before analyzing the coupling caused by the current distribution in each mode in Fig. 7(a). The effects caused by coupling other than the mutual inductance analyzed below are disregarded to avoid difficulty in calculating the segments [23] owing to the relatively large effective distance and other field interference caused by the adjacent segments.

1) *Mutual Inductance Case 1—Parallel Line*: The analysis of parallel line mutual inductance is performed for the segments of the outer and inner windings and the same procedure is applied when considering the inner and center windings. Fig. 7(b) shows a diagram wherein the segments of different lengths are arranged in parallel and aligned in the center. Each segment length  $l$  can be expressed as the diameter of the

corresponding winding using (7). The geometric mean distance (GMD) between the two windings can be expressed as

$$\ln(\text{GMD}_{oi}) = \ln(P) - \frac{W^2}{12P^2}. \quad (8)$$

Considering that the practical ratio of the segment pitch  $P$ , and  $W$  is larger than 1.4. The mutual inductance for the parallel case  $M_{par}$  can be calculated as [24]

$$M_{par} = M_{long} - M_{short} \quad (9)$$

where

$$M_{long} = (l_{out} + l_{in}) \left( \ln \left[ \frac{l_{out} + l_{in}}{2\text{GMD}_{oi}} + \sqrt{1 + \left( \frac{l_{out} + l_{in}}{2\text{GMD}_{oi}} \right)^2} \right] - \sqrt{1 + \left( \frac{2\text{GMD}_{oi}}{l_{out} + l_{in}} \right)^2} + \frac{2\text{GMD}_{oi}}{l_{out} + l_{in}} \right) \quad (10)$$

$$M_{short} = (l_{out} - l_{in}) \left( \ln \left[ \frac{l_{out} - l_{in}}{2\text{GMD}_{oi}} + \sqrt{1 + \left( \frac{l_{out} - l_{in}}{2\text{GMD}_{oi}} \right)^2} \right] - \sqrt{1 + \left( \frac{2\text{GMD}_{oi}}{l_{out} - l_{in}} \right)^2} + \frac{2\text{GMD}_{oi}}{l_{out} - l_{in}} \right). \quad (11)$$

Utilizing the predefined assumptions,  $M_{par}$  can be simplified as

$$M_{par} = C_1 u \left( \ln \left[ \frac{u}{v} \right] - \left( C_2 \frac{v}{u} + C_3 \right)^2 + C_4 \right) + C_5 v \quad (12)$$

where  $u$  and  $v$  denote the sum and difference of the outer and inner winding diameters, respectively, and  $C_i$  ( $i = 1$  to 5) represents a constant coefficient without any geometric parameters.

2) *Mutual Inductance Case 2—135° Connected*: Fig. 7(c) shows the case where two segments are connected to one side of the other at an angle of 135°. The formula is derived for the outer winding, and the same method can be applied to the inner or center winding. The mutual inductance between the connected segments  $M_{conn}$  is expressed as

$$M_{conn} = 4 l_{out} \cos \theta \tanh^{-1} \left( \frac{l_{out}}{l_{out} + r_1} \right) \quad (13)$$

where

$$r_1^2 = 2 l_{out}^2 (1 - \cos \theta). \quad (14)$$

Considering that  $\theta$  has a value of 135° for an octagonal inductor shape,  $M_{conn}$  can be simplified as

$$M_{conn} = C(u + v). \quad (15)$$

Like in the parallel segment case,  $C$  is a constant that does not contain any geometric parameters. When considering the mutual coupling between the connected segments for the inner and center windings, the term  $u + v$  in  $M_{conn}$  should be substituted with  $u - v$  and  $l_c$ , respectively.

3) *Mutual Inductance Case 3—45° Coupled*: Fig. 7(d) shows an example of a case in which each segment corresponding to a part of the outer and inner windings is spaced apart by pitch,  $P_{oi}$ , and couples at a specific angle. For an octagonal inductor structure,  $\theta_1$  is  $45^\circ$ , and  $\theta_2$  is  $67.5^\circ$ . It is necessary to divide the outer segment into two parts based on the point where the inner segment intersects when extended to obtain the mutual inductance given an angle,  $M_{coup}$

$$M_{coup} = M_{coup1} + M_{coup2}. \quad (16)$$

The mutual inductances of the relatively long and short parts of the outer segment separated based on the intersection of the inner segment are called  $M_{coup1}$  and  $M_{coup2}$ , respectively. The ratio of the separated lengths is expressed as

$$\frac{l_1}{l_2} = \frac{1}{\sqrt{2}} \left( \frac{(\sqrt{2}-1)u}{v} + 1 \right) \quad (17)$$

where  $l_1$  and  $l_2$  represent the lengths of the long and short parts, respectively. Applying the relation  $u/v \gg 1$  for tightly coupled condition to (17), it can be said that  $M_{coup2}$  can be neglected when comparing to  $M_{coup1}$ . Such as the parallel segment case,  $M_{coup1}$  can be expressed as

$$M_{coup1} = -2 \cos \theta_1 \left[ (R_3 + l_{in}) \tanh^{-1} \left( \frac{l_1}{R_1 + R_2} \right) + l_1 \tanh^{-1} \left( \frac{l_{in}}{R_1 + R_4} \right) - R_3 \tanh^{-1} \left( \frac{l_1}{R_3 + R_4} \right) \right] \quad (18)$$

where

$$R_1 = (\sqrt{2}-1)u \quad (19)$$

$$R_2 = \frac{(\sqrt{2}-1)u + v}{2} \quad (20)$$

$$R_3 = \frac{v}{\sqrt{2}} \quad (21)$$

$$R_4 = \frac{\sqrt{2}-1}{2}(u+v). \quad (22)$$

Because all expressions inside the  $\tanh^{-1}$  function are less than 1 in the tightly coupled condition,  $M_{coup}$  can be simplified as shown below through a Taylor's series expansion

$$M_{coup} = C' \frac{u-v}{3u+v} \{u - (1 + \sqrt{2})v\} \cdot \frac{42u^2 + (38 + 13\sqrt{2})uv + (6 + 5\sqrt{2})v^2}{\{(3\sqrt{2}-3)u + v\}\{(3 + \sqrt{2})u + v\}} \quad (23)$$

where  $C'$  denotes a constant coefficient without geometric parameters.

The equivalent circuit can be analyzed in detail for each mode of operation based on the parasitic capacitance, resistance, self-inductance, and mutual inductance derived from the geometric parameters. Fig. 8(a) shows each self-inductance and mutual inductance in the equivalent circuit for odd and even modes based on the segment model.  $L_{so}$  and  $L_{si}$  represent the segment self-inductance of the outer and inner windings, respectively, and it can be obtained through (4).  $M_{conno}$  and

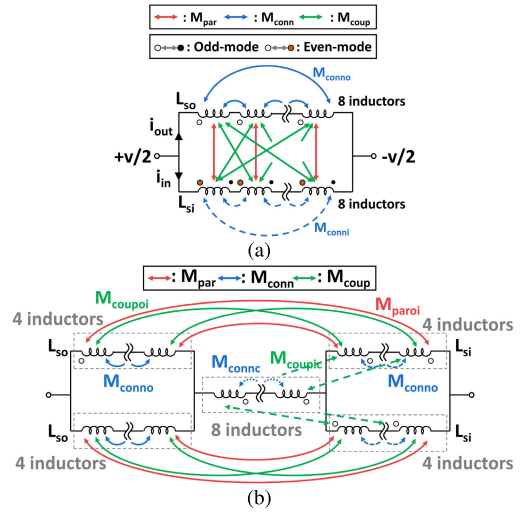


Fig. 8. (a) Odd- and even-mode and (b) expansion-mode equivalent circuits with the segmented model, which shows self- and mutual-inductances.

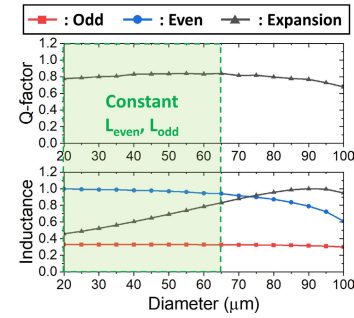


Fig. 9. Normalized inductance and  $Q$ -factor for the expansion mode with respect to the change in the center winding diameter.

$M_{conni}$  are mutual inductances for the connected case between the outer and inner segments, respectively, and they are obtained using (15). Only three of the eight segments of each outer and inner winding are shown to make the circuit more notable. The relationship between the voltage across the entire circuit and the current flowing along each winding is expressed as

$$\begin{pmatrix} v \\ v \end{pmatrix} = \begin{pmatrix} 8 L_{so} \mp 16 M_{conno} & \mp 3 M_{paroi} \mp 6 M_{coupoi} \\ \mp 3 M_{paroi} \mp 6 M_{coupoi} & 8 L_{si} \mp 16 M_{conni} \end{pmatrix} \times \begin{pmatrix} di_{out}/dt \\ di_{in}/dt \end{pmatrix}. \quad (24)$$

The sign before the mutual inductances corresponds to minus for the odd mode and plus for the even mode. Through (1), (2), and (24), the odd- and even-mode inductances based on the segment model are given below

$$L_{odd/even} = \frac{8\{(L_{so} \mp 2 M_{conno})(L_{si} \mp 2 M_{conni}) - (M_{paroi} + 2 M_{coupoi})^2\}}{L_{so} + L_{si} \mp (M_{conno} + M_{conni} - M_{paroi} - 4 M_{coupoi})}. \quad (25)$$

Fig. 8(b) shows an equivalent circuit showing each self-inductance and mutual inductance in the expansion mode reflecting the segment model. The subscripts  $o$ ,  $i$ , and  $c$  correspond to the outer, inner, and center windings, respectively,

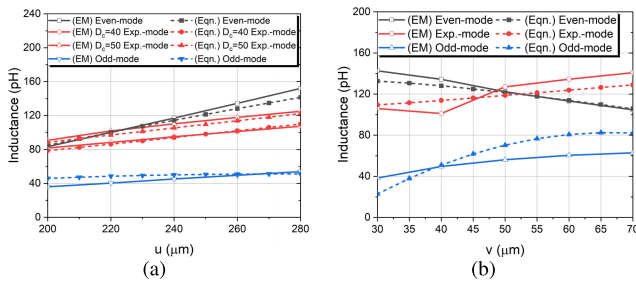


Fig. 10. Comparison of inductances for each mode extracted from the EM simulation and derived from the equation according to (a)  $u$  and  $D_c$ , and (b)  $v$ .

and  $o_i$  and  $i_c$  refer to the interaction between the outer inner and inner center windings. Based on the inductance and  $Q$ -factor obtained in the equivalent circuit of each mode, the effect of changing the diameter of the center winding in the expansion mode is shown in Fig. 9. A change in the center winding is performed for the dimension with an average diameter of  $110 \mu\text{m}$  and a gap of  $12 \mu\text{m}$  for the outer and inner windings. As expected, for the region where the other odd- and even-mode inductances are relatively constant based on the current distribution, the expansion-mode inductance is proportional to the diameter. However,  $L_{\text{odd}}$  and  $L_{\text{even}}$  decrease at diameters over  $65 \mu\text{m}$ , and at  $100 \mu\text{m}$ , 39% and 10% reductions occurred, respectively. The reduced inductance deteriorates the  $Q$ -factor because there is no significant change in the series resistance value for the odd and even modes. It is not practical to use a region in which the inductance of each mode decreases because it is desirable to use an inductor component with a high  $Q$ -factor when designing a VCO.

### C. Comparison With EM Results

A comparison was done with the EM results to confirm the validity of the inductance formula for each mode derived from the geometric parameters. Equivalent circuit in Fig. 8(b) and (25) are used to calculate expansion- and even-/odd-mode inductances, respectively. Fig. 10(a) compares the effects of changes in  $u$  and  $D_c$  on inductance when  $v$  is fixed at  $50 \mu\text{m}$ . For  $u$  above  $240 \mu\text{m}$ , the EM and calculated results show good agreement with differences within 10% in all modes. Also, only the expansion mode inductance increases when  $D_c$  is increased for a fixed  $u$ . However, as  $u$  gets smaller the difference between the EM and calculated results is widened due to the gap between windings decreases so that the mutual inductance between outer and center windings can no longer be neglected. But these  $u$  regions are not used in the practical design because the expansion-mode inductance is similar to or greater than the even-mode inductance. Fig. 10(b) plots the inductance of each mode according to  $v$  change for fixed  $u$  and  $D_c$ . Contrary to the  $u$  trend, the difference between the EM and the calculation result occurs as  $v$  becomes larger than  $50 \mu\text{m}$ . However, it is not practical to use large  $v$  value, since the expansion and even mode inductances are similar for  $v$  is near  $50 \mu\text{m}$ , and the difference in inductance between even and odd modes becomes smaller for near  $70 \mu\text{m}$ . Therefore, it is sufficient to design the SMCI for use in a tri-band VCO

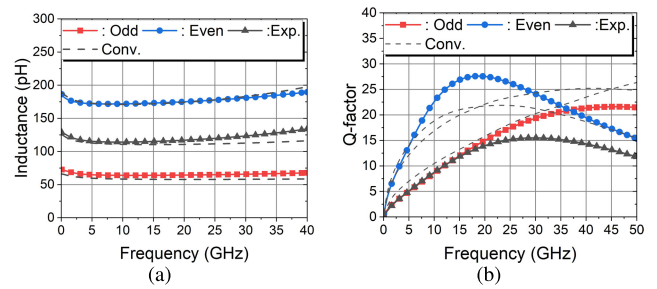


Fig. 11. (a) Inductance and (b)  $Q$ -factor for each mode in the optimized structure.

based on the equations derived from the geometric parameters in Section II-B then finetuned by EM simulation.

Fig. 11(a) and (b) show the EM simulation result of inductance and  $Q$ -factor according to frequency, respectively, when the proposed structure is optimized through the equation and fine-tuning. Also, comparisons with conventional inductor structures with similar inductance have been added. For the target frequency bands corresponding to the  $Ku$ -,  $K$ -, and  $Ka$ -bands, the optimized ratios of the even, expansion, and odd mode inductances of SMCI are 1, 0.6, and 0.35, respectively. Owing to the inductance relationship for each mode, VCO operates in the low, mid, and high bands when the SMCI operates in the even, expansion, and odd modes. In addition, it can be confirmed that the maximum  $Q$ -factor for each corresponding mode occurs in the target frequency band.

## III. PROOF OF CONCEPT IMPLEMENTATIONS

### A. Fundamental of Tri-Band Oscillation

A schematic of a tri-band VCO based on an optimized SMCI and oscillation cores is shown in Fig. 12. The VCO has a total of three cores, each of which provides a negative transconductance ( $G_m$ ) and capacitance for oscillation through a varactor and cross-coupled topology. The drain node of each core is connected to the node of the adjacent core. The connection between the four RF ports of SMCI is changed for mode operation by applying a switch between each drain node. A total of six switches are used to implement the three modes with two pairs, and the switches turned on during the odd, even, and expansion mode operations of the inductor are  $SW_{\text{odd}}$ ,  $SW_{\text{even}}$ , and  $SW_{\text{exp}}$ , respectively. The operating band of the VCO is determined by controlling the ON/OFF-state of the switches and cores through a proper bias level, as indicated in Table II. When the inductor operates in the even and odd modes, VCO uses both core1 and core3 simultaneously to oscillate in the high and low bands, respectively. Therefore, the transistors  $M_{N1}$  and  $M_{N3}$  used in core1 and 3, respectively, must have the same size to maintain the symmetry of the generated negative  $G_m$ . In the mid-band oscillation, only core2 is used as opposed to the operations of the previous two bands; therefore, the transistor of core2,  $M_{N2}$ , is 1.33 times larger than  $M_{N1}$  to generate comparable  $G_m$ . The exact parameter values in the SMCI and the components used in the VCO are listed in Table III.

Connecting a switch directly to the VCO core is not preferred because it causes phase noise deterioration and a

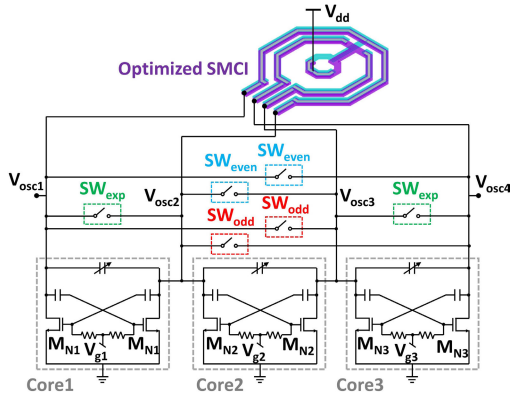


Fig. 12. Schematic of proposed tri-band VCO with three cores with optimized SMCI and paired switches.

TABLE II  
BIAS LEVEL FOR EACH VCO OPERATION BAND

	Low-band (Even)	Mid-band (Expansion)	High-band (Odd)
$V_{g1}$	High	Low	High
$V_{g2}$	Low	High	Low
$V_{g3}$	High	Low	High
$SW_{odd}$	Low	Low	High
$SW_{even}$	High	Low	Low
$SW_{exp}$	Low	High	Low

TABLE III  
PARAMETRIC VALUES OF SMCI AND VCO

Parameter	Value
$D_c$	45 $\mu\text{m}$
$D_{in}$	120 $\mu\text{m}$
$D_{out}$	150 $\mu\text{m}$
$W_c, W_{in}, W_{out}$	9 $\mu\text{m}$
$M_{N1}, M_{N3}$ total width	18 $\mu\text{m}$
$M_{N2}$ total width	24 $\mu\text{m}$
$SW$ width	4 $\mu\text{m}$

reduced FTR because of the added parasitic resistance and capacitance [25], [26]. There exists a trade-off between the degradation effect on the phase noise and the FTR because the ON-resistance and OFF-capacitance of a switch are inversely proportional [27]. This study mitigates the switch degradation effect by splitting the core into three, which eliminates the effect of the ON-resistance of the switch for all-band operation, as shown in Fig. 13. For all modes, the effect on phase noise can be neglected because no current flows through the ON-resistance and the same polarity potential is applied to both ends of the ON-state switch. The oscillation frequency of the proposed VCO for each mode is only affected by the switch-OFF-capacitance; it is expressed as

$$f_{\text{low}} = \frac{1}{2\pi\sqrt{L_{\text{even}}(2C_{\text{var}} + 4C_{\text{SW}})}} \quad (26)$$

$$f_{\text{high}} = \frac{1}{2\pi\sqrt{L_{\text{odd}}(2C_{\text{var}} + 4C_{\text{SW}} + C_{\text{core2}})}} \quad (27)$$

$$f_{\text{mid}} = \frac{1}{2\pi\sqrt{L_{\text{exp}}(2C_{\text{var}} + 4C_{\text{SW}})}} \quad (28)$$

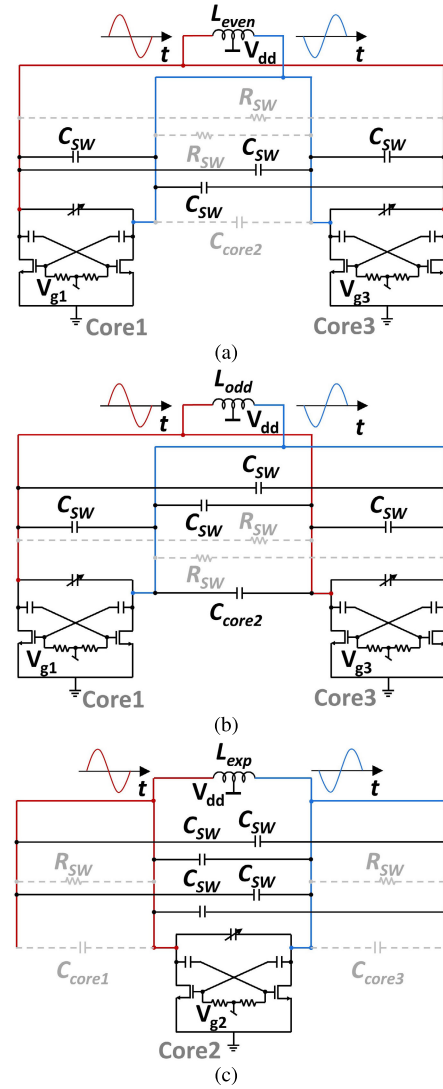


Fig. 13. Equivalent circuit and generated differential signal according to the state of the cores and switches for (a) low-, (b) high-, and (c) mid-band operations.

where  $C_{\text{var}}$  denotes the capacitance of the varactor loaded into each core,  $C_{\text{SW}}$  denotes the OFF-capacitance of the switch, and  $C_{\text{core2}}$  denotes the parasitic capacitance when core2 is OFF. A small switch is used to minimize the FTR reduced by the  $C_{\text{SW}}$  because it is confirmed that there is no performance degradation due to the switch ON-resistance. According to (26) and (27), the frequency ratio of the low and high bands is not exactly determined by the even- and odd-mode inductances of an inductor. In the low-band mode,  $C_{\text{core2}}$  can be neglected; however, for the high-band mode, a potential difference occurs across both ends, which affects the oscillation frequency. Therefore, it is necessary to compensate for the mismatch in the VCO oscillation frequency ratio by deriving the ratio of  $L_{\text{even}}$  and  $L_{\text{odd}}$  considering  $C_{\text{core2}}$  in the optimization process in Section II-C.

### B. SMCI-Coupled Switch Effect

The difference in phase noise according to the presence or absence of switches coupled to SMCI is analyzed based on

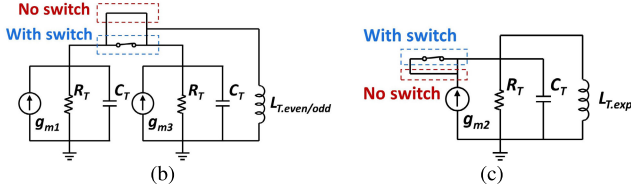
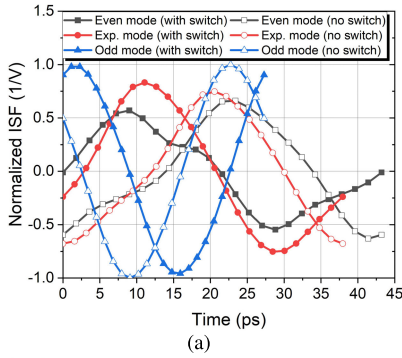


Fig. 14. (a) Normalized ISF results and (b) and (c) small-signal equivalent model for each oscillation mode.

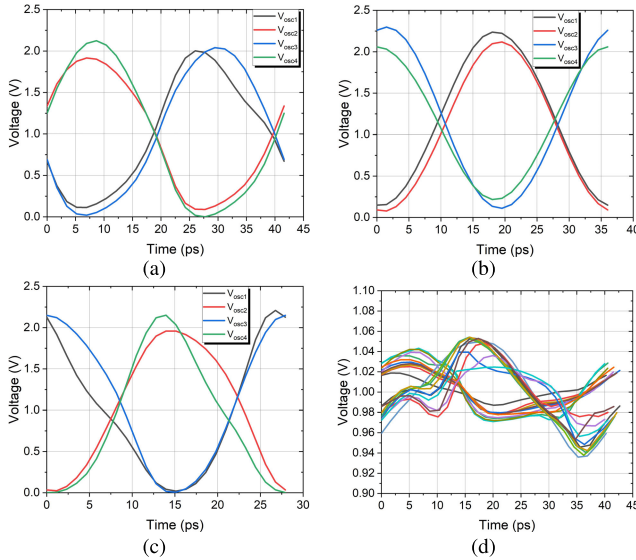


Fig. 15. Simulated voltage swing of the four VCO oscillation nodes for (a) even-, (b) expansion-, and (c) odd-mode. (d) Source-gate and drain-gate voltage difference graph formed on the switch according to the varactor tuning voltage.

the time domain impulse sensitivity function (ISF) [28], [29]. The simulated results of normalized ISF for each mode are plotted in Fig. 14(a) using periodic steady-state analysis in Cadence. It shows that the differences between ISFs are within 10% when the switch is coupled and replaced with shorted circuit [see Fig. 14(b) and (c)] for all modes. To compensate for the low  $Q$ -factor of the expansion mode inductance, the expansion operated ISF is designed to be similar to the other two modes by taking into account the  $g_{m2}$  of core2, which uses a 1.33 times larger transistor. The simulated even, odd, and expansion mode operation frequencies are 23.1, 26.3, and 38.2 GHz, respectively.

When the oscillator falls into a steady state for all modes, the oscillation voltage swing at each node are formed as shown in Fig. 15. For the even mode, the voltages across the ON-

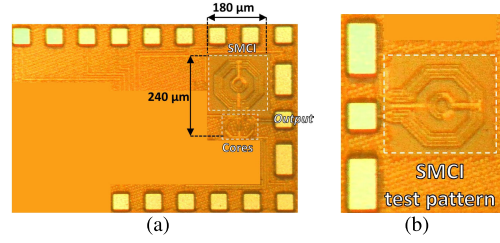


Fig. 16. Die micrograph of proposed (a) tri-band VCO and (b) SMCI test patterns and the Samsung 28-nm bulk complementary metal-oxide-semiconductor (CMOS) technology occupying 0.043 mm<sup>2</sup>.

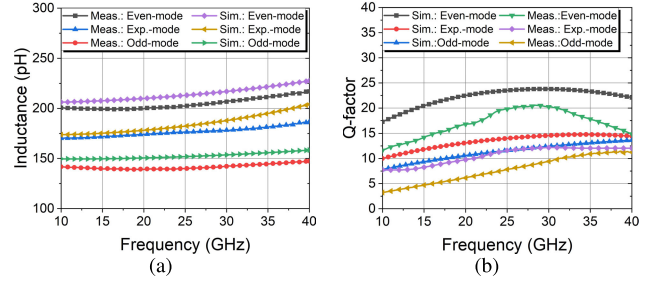


Fig. 17. (a) Inductance and (b)  $Q$ -factor measurement results for the inductor test pattern.

switches for mode operation are  $V_{Osc1}$ ,  $V_{Osc3}$  and  $V_{Osc2}$  and  $V_{Osc4}$ , respectively. The voltage difference between the source and drain of the nMOS switch is within 0.1 V on average in one cycle. Therefore, the effect on the ISF is insignificant as the current flowing through the ON-switch is negligible. Also, it is ensured not to exceed the breakdown voltage of the transistor through a large resistor with a dc voltage of 0 V in the OFF-state and 2 V in the ON-state to secure the reliability. The voltage differences between the gate–source and gate–drain are formed across switch transistors with are maximum of 1.05 V for all varactor tuning voltages.

#### IV. MEASUREMENT RESULTS

The die micrograph of the proposed SMCI test patterns and proposed tri-band VCO fabricated using a Samsung 28-nm bulk CMOS process is shown in Fig. 16. The area occupied only by the inductor component and the oscillation cores excluding the bias and output pads was 0.043 mm<sup>2</sup>.

Fig. 17 shows the inductance and  $Q$ -factor results based on the test pattern measurements of the fabricated SMCI. For measurement according to the odd, even, and expansion modes, the measurements were conducted using test patterns where four RF ports of the SMCI were connected appropriately for each mode operation. Pad deembedding was performed to extract the characteristics of the proposed SMCI while excluding the impedance change caused by the pad. The inductor designed through the optimization shows inductances of 199.3, 174.5, and 154.3 pH in the even, expansion, and odd modes, with the frequencies with corresponding  $Q$ -factors at the maximum at 19.1, 23.3, and 34.8 GHz, respectively.

Fig. 18 shows the FTR for each band measured according to the mode operation with a  $V_{dd}$  of 1.2 V. The oscillation frequency varies according to the voltage formed in the varactor of the turned-on core,  $V_{tune}$ , and the operating state of each

TABLE IV  
COMPARISON OF THE TRI-BAND VCO WITH THE STATE-OF-THE-ART VCOS

Reference	Type	Process (CMOS)	Frequency (GHz)	Tuning Range (%)	$PN_{norm}^*$ (dBc/Hz)	$V_{tune}$ range (V)	$V_{DD}$ (V)	$P_{DC}$ (mW)	$FoM^{**}$ (dBc/Hz)	$FoM_T^{***}$ (dBc/Hz)	Size (mm <sup>2</sup> )
TMTT'12 [30]	Dual-band	180-nm	10.7 / 22	7.6 / 8	-196.5 / -193.6 <sup>§</sup>	3.6	1.8	15.2	-184.6 / -181.8	-182.2 / -179.9	0.75
MWCL'14 [13]	Tri-band	180-nm	3.49 / 7.53 / 8.51	24.2 / 2.91 / 6.35	-193.9 / -197.1 / -196.9 <sup>§</sup>	2	0.65	3.83	-188.7 / -191.1 / -190.7	-196.4 / -180.4 / -186.8	0.57
BCTM'16 [31]	Tri-band	0.25- $\mu$ m SiGe:C	18 / 36 / 67	9.5 / 9.5 / 9.5	-198.4 / -198.8 / -196.5 <sup>§</sup>	5	2.5	95	-178.6 / -179.1 / -176.7	-178.1 / -178.6 / -176.3	0.329
ISSCC'18 [32]	Single-band	130-nm BiCMOS	15	16	-207.5 <sup>§</sup>	3.6	3	72	-189	-193	1
RFIC'18 [33]	Dual-band	28-nm	26.25	43.3	-193.4 <sup>  </sup>	1	0.9	5.5	-183.3	-195.8	0.067
ISSCC'19 [34]	Single-band	65-nm	27.7	16	-202.9 <sup>  </sup>	1.2	0.48	3.8 - 4	-191.6	-195.7	0.08
TMTT'19 [35]	Dual-band	65-nm	16.75 / 23.7	23.3 / 24.4	-192.5 / -194.1 <sup>†§</sup>	30 codes	0.75	4.8	-187.6 / -187.2	-195.1 / -194.9	0.046
RFIC'20 [36]	Tri-band	22-nm FDSOI	12.5	72	-205 / -174.3 <sup>  </sup>	2.4	0.45	17 - 33	-191.7 / -180.7	-208.8 / -197.8	0.39
IMS'20 [37]	Tri-band	65-nm	19 / 28 / 36	12.1 / 9 / 12.5	-192.8 / -190.0 / -191.5 <sup>§</sup>	0.7	1.2	10 - 12	-187.5 / -184.5 / -186.1	-194.8	0.0875
ISSCC'20 [38]	Quad-band	40-nm	29.35	73.2	-199.7 to -192.1 <sup>  </sup>	2.2	1.1	9 - 15	-186.3 to -183.0	-203.6 to -200.3	0.08
ISSCC'21 [39]	Single-band	65-nm	56.4	14.2	-199.7 <sup>§</sup>	7 codes	0.55	22.5 - 23.6	-186.5	-189.5	0.032
<b>This Work</b>	Tri-band	28-nm	18.4 / 23.8 / 35.1	17.5 / 16.5 / 17.9	-194.8 / -195.7 / -193.4 <sup>†</sup>	2.5	1.2	11.6 / 15 / 11.6	-184.1 / -184.0 / -182.8	-189.0 / -188.3 / -187.8	0.043

\*:  $PN_{norm} = L\{\Delta f\} - 20 \log(f_{osc}/\Delta f)$ ; \*\*:  $FoM = PN_{norm} + 10 \log(P_{DC}/1mW)$ ; \*\*\*:  $FoM_T = FoM - 20 \log(10 \cdot FTR)$  †: Peak performance; ‡: Average performance. §: 1-MHz offset frequency ||: 10-MHz offset frequency

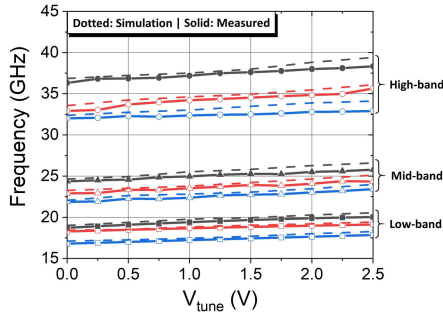


Fig. 18. Measured FTR for low-, mid-, and high-band operations.

core is determined by the voltage applied to the gate based on the threshold voltage. Fine frequency tuning is achieved by controlling the voltage,  $V_{fine}$ , on the varactor connected to the off-core, which does not contribute to the oscillation. The frequency ranges measured in the low, mid, and high bands are 16.79–20 GHz (17.5%), 21.87–25.8 GHz (16.5%), and 32.01–38.3 GHz (17.9%), respectively. The phase noise measurement results and figure-of-merit (FoM) for the tri-band operation of the proposed VCO are shown in Fig. 19. At 10-MHz offset frequency, it shows a minimum of  $-129.5$ ,  $-128.2$ , and  $-122.5$  dBc/Hz in the low, mid, and high bands, respectively. The corresponding minimum FoM for each mode is  $-184.2$ ,  $-182.3$ , and  $-184.5$  dBc/Hz, respectively.

Table IV compares the performance capabilities of the proposed topology with the state-of-the-art dual- and tri-band VCOs. For comparison, the normalized phase noise ( $pn_{norm}$ ),

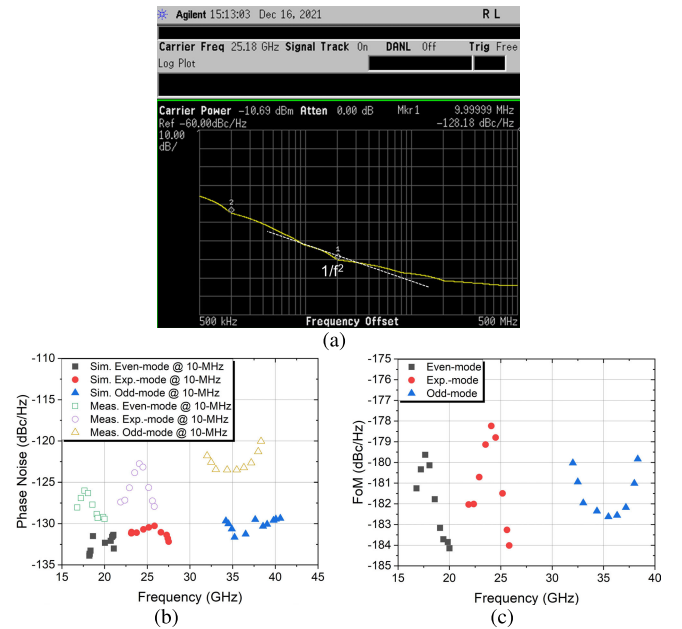


Fig. 19. Measured phase noise (a) at 25.2 GHz, and (b) for low-, mid-, and high-band operation. (c) FoM plot for each mode according to varactor tuning voltage.

phase noise FoM, and  $FoM_T$  with phase noise and an FTR are used. The proposed tri-band VCO achieves excellent  $FoM_T$  outcomes for all three modes. Considering the ratio of the area occupied by VCO to the frequency, it was confirmed that the proposed SMCI could achieve the most miniaturized area with

the tri-band operation. To the best of the authors' knowledge, the proposed VCO achieves the best average FoM<sub>T</sub> in silicon on *K*- and *Ka*-bands with the tri-band operation.

## V. CONCLUSION

In this study, SMCI based on a multiwinding structure without any extra inductive element was first presented in VCO to achieve a performance comparable to that of other multiband techniques while consuming a compact chip area. The measurement shows an average FoM<sub>T</sub> of  $-188.4$  dBc/Hz for frequencies of 18.4, 23.8, and 35.1 GHz. The resulting circuit consumes the smallest area among the state-of-the-art mmWave tri-band VCOs with an FoM<sub>T</sub> of better than  $-187$  dBc/Hz for all bands. The odd, even, and expansion modes of SMCI are realized by changing the excitation of each port. The self-inductance and mutual inductance of SMCI for each mode are determined by the current path and direction flowing through the windings. Through equivalent circuit and geometric parameter analysis, this study showed that the inductance of each mode could be designed independently and allows the optimization for the three target frequency bands. The proposed SMCI is not limited to VCO implementation, but it can also be used for multiband matching to design various miniaturized circuits for multiband applications. Multiple cores and paired switches are used to avoid performance degradation during reconfigurable operation for tri-band implementation. When multiple amplifying transistor cells with a differential structure are applied, proposed SMCI can be a sufficiently practical approach for multiband amplifiers.

## ACKNOWLEDGMENT

The EDA tool was supported by the IC Design Center (IDEC), Korea.

## REFERENCES

- [1] Y. Wang, J. Li, L. Huang, Y. Jing, A. Georgakopoulos, and P. Demestichas, "5G mobile: Spectrum broadening to higher-frequency bands to support high data rates," *IEEE Veh. Technol. Mag.*, vol. 9, no. 3, pp. 39–46, Sep. 2014.
- [2] A. N. Uwaechia and N. M. Mahyuddin, "A comprehensive survey on millimeter wave communications for fifth-generation wireless networks: Feasibility and challenges," *IEEE Access*, vol. 8, pp. 62367–62414, 2020.
- [3] Z. Pi and F. Khan, "An introduction to millimeter-wave mobile broadband systems," *IEEE Commun. Mag.*, vol. 49, no. 6, pp. 101–107, Jun. 2011.
- [4] A. Valdes-Garcia et al., "Single-element and phased-array transceiver chipsets for 60-GHz Gb/s communications," *IEEE Commun. Mag.*, vol. 49, no. 4, pp. 120–131, Apr. 2011.
- [5] H.-T. Kim et al., "A 28-GHz CMOS direct conversion transceiver with packaged 2×4 antenna array for 5G cellular system," *IEEE J. Solid-State Circuits*, vol. 53, no. 5, pp. 1245–1259, May 2018.
- [6] E. A. Abbas, M. Ikram, A. T. Mobashsher, and A. Abbosh, "MIMO antenna system for multi-band millimeter-wave 5G and wideband 4G mobile communications," *IEEE Access*, vol. 7, pp. 181916–181923, 2019.
- [7] A. I. Sandhu, E. Arneri, G. Amendola, L. Boccia, E. Meniconi, and V. Ziegler, "Radiating elements for shared aperture Tx/Rx phased arrays at K/Ka band," *IEEE Trans. Antennas Propag.*, vol. 64, no. 6, pp. 2270–2282, Jun. 2016.
- [8] J. Borremans et al., "A compact wideband front-end using a single-inductor dual-band VCO in 90 nm digital CMOS," *IEEE J. Solid-State Circuits*, vol. 43, no. 12, pp. 2693–2705, Dec. 2008.
- [9] R. Sathwani, A. Ben Bassat, A. A. Kidwai, and S. Rivel, "Multi-band multi-standard local oscillator generation for direct up/down conversion transceiver architectures supporting WiFi and WiMAX bands in standard 45 nm CMOS process," in *Proc. IEEE Radio Freq. Integr. Circuits Symp.*, May 2010, pp. 149–152.
- [10] A. Tanabe, K. Hijioka, H. Nagase, and Y. Hayashi, "A low-power, small area quadrature LC-VCO using miniature 3D solenoid shaped inductor," in *Proc. IEEE Radio Freq. Integr. Circuits Symp.*, Jun. 2009, pp. 263–266.
- [11] A. Kral, F. Behbahani, and A. A. Abidi, "RF-CMOS oscillators with switched tuning," in *Proc. IEEE Custom Integr. Circuits Conf. (CICC)*, May 1998, pp. 555–558.
- [12] H. Shin, Z. Xu, and M. F. Chang, "A 1.8-V 6/9-GHz switchable dual-band quadrature LC VCO in SiGe BiCMOS technology," in *Proc. IEEE Radio Freq. Integr. Circuits Symp. (RFIC)*, Jun. 2002, pp. 71–74.
- [13] S. Jain and S.-L. Jang, "Triple-band transformer-coupled LC oscillator with large output voltage swing," *IEEE Microw. Wireless Compon. Lett.*, vol. 24, no. 7, pp. 475–477, Jul. 2014.
- [14] H. Krishnaswamy and H. Hashemi, "Inductor- and transformer-based integrated RF oscillators: A comparative study," in *Proc. IEEE Custom Integr. Circuits Conf. (CICC)*, Sep. 2006, pp. 381–384.
- [15] B. Li, Y. Liu, C. Yu, and Y. Wu, "Independent control function for concurrent dual-band VCO," *IEEE Microw. Wireless Compon. Lett.*, vol. 28, no. 3, pp. 230–232, Mar. 2018.
- [16] J. Shi, K. Kang, Y. Z. Xiong, J. Brinkhoff, F. Lin, and X. J. Yuan, "Millimeter-wave passives in 45-nm digital CMOS," *IEEE Electron Device Lett.*, vol. 31, no. 10, pp. 1080–1082, Oct. 2010.
- [17] Y. Cao et al., "Frequency-independent equivalent-circuit model for on-chip spiral inductors," *IEEE J. Solid-State Circuits*, vol. 38, no. 3, pp. 419–426, Mar. 2003.
- [18] C.-H. Wu, C.-C. Tang, and S.-I. Liu, "Analysis of on-chip spiral inductors using the distributed capacitance model," *IEEE J. Solid-State Circuits*, vol. 38, no. 6, pp. 1040–1044, Jun. 2003.
- [19] H. M. Greenhouse, "Design of planar rectangular microelectronic inductors," *IEEE Trans. Parts, Hybrids, Packag.*, vol. PHP-10, no. 2, pp. 101–109, Jun. 1974.
- [20] K. B. Ashby, I. A. Koullias, W. C. Finley, J. J. Bastek, and S. Moinian, "High *Q* inductors for wireless applications in a complementary silicon bipolar process," *IEEE J. Solid-State Circuits*, vol. 31, no. 1, pp. 4–9, Jan. 1996.
- [21] T. Lee, *The Design of CMOS Radio-Frequency Integrated Circuits*. Cambridge, U.K.: Cambridge Univ. Press, 2003.
- [22] C. P. Yue and S. S. Wong, "Physical modeling of spiral inductors on silicon," *IEEE Trans. Electron Devices*, vol. 47, no. 3, pp. 560–568, Mar. 2000.
- [23] I. Bahl, *Lumped Elements for RF and Microwave Circuits* (Artech House Microwave Library). Norwood, MA, USA: Artech House, 2003.
- [24] F. Grover, *Inductance Calculations: Working Formulas and Tables* (Dover Books for Engineers). New York, NY, USA: Dover, 1946.
- [25] M. Kossel, T. Morf, P. Buchmann, M. L. Schmatz, C. Menolfi, and T. Toifl, "Switched inductor with wide tuning range and small inductance step sizes," *IEEE Microw. Wireless Compon. Lett.*, vol. 19, no. 8, pp. 515–517, Aug. 2009.
- [26] Y.-C. Chiang, J.-C. Chen, and Y.-H. Chang, "A study on the variable inductor design by switching the main paths and the coupling coils," *Electronics*, vol. 10, no. 15, p. 1856, Aug. 2021. [Online]. Available: <https://www.mdpi.com/2079-9292/10/15/1856>
- [27] M. Kucharski, F. Herzel, H. J. Ng, and D. Kissinger, "A Ka-band BiCMOS LC-VCO with wide tuning range and low phase noise using switched coupled inductors," in *Proc. IEEE Eur. Microw. Integr. Circuits Conf. (EuMIC)*, Oct. 2016, pp. 201–204.
- [28] D. Murphy, J. J. Rael, and A. A. Abidi, "Phase noise in LC oscillators: A phasor-based analysis of a general result and of loaded *Q*," *IEEE Trans. Circuits Syst. I, Reg. Papers*, vol. 57, no. 6, pp. 1187–1203, Jun. 2010.
- [29] A. Mazzanti and P. Andreani, "Class-C harmonic CMOS VCOs, with a general result on phase noise," *IEEE J. Solid-State Circuits*, vol. 43, no. 12, pp. 2716–2729, Dec. 2008.
- [30] S. L. Liu, K. H. Chen, and A. Chin, "A dual-resonant mode 10/22-GHz VCO with a novel inductive switching approach," *IEEE Trans. Microw. Theory Techn.*, vol. 60, no. 7, pp. 2165–2177, Jul. 2012.

- [31] D. Cabrera, J. Begueret, N. Verrascina, O. Tesson, O. Mazouffre, and P. Gamand, "A low phase noise tri-band LO generation for Ku and E band radios for backhauling point-to-point applications," in *Proc. IEEE Bipolar/BiCMOS Circuits Technol. Meeting (BCTM)*, Sep. 2016, pp. 56–59.
- [32] F. Padovan, F. Quadrelli, M. Bassi, M. Tiebout, and A. Bevilacqua, "A quad-core 15 GHz BiCMOS VCO with  $-124$  dBc/Hz phase noise at 1 MHz offset,  $-189$  dBc/Hz FOM, and robust to multimode concurrent oscillations," in *IEEE Int. Solid-State Circuits Conf. (ISSCC) Dig. Tech. Papers*, Feb. 2018, pp. 376–378.
- [33] Y. Shu, H. J. Qian, and X. Luo, "A 20.7–31.8 GHz dual-mode voltage waveform-shaping oscillator with 195.8 dBc/Hz FoMT in 28 nm CMOS," in *Proc. IEEE Radio Freq. Integr. Circuits Symp. (RFIC)*, Jun. 2018, pp. 216–219.
- [34] H. Guo, Y. Chen, P.-I. Mak, and R. P. Martins, "A 0.08 mm<sup>2</sup> 25.5-to-29.9 GHz multi-resonant-RLCM-tank VCO using a single-turn multi-tap inductor and CM-only capacitors achieving 191.6 dBc/Hz FoM and 130 kHz  $1/f^3$  PN corner," in *IEEE Int. Solid-State Circuits Conf. (ISSCC) Dig. Tech. Papers*, Feb. 2019, pp. 410–412.
- [35] J. Baylon, P. Agarwal, L. Renaud, S. N. Ali, and D. Heo, "A Ka-band dual-band digitally controlled oscillator with  $-195.1$  dBc/Hz FoM<sub>T</sub> based on a compact high- $Q$  dual-path phase-switched inductor," *IEEE Trans. Microw. Theory Techn.*, vol. 67, no. 7, pp. 2748–2758, Jul. 2019.
- [36] O. El-Aassar and G. M. Rebeiz, "A dual-core 8–17 GHz LC VCO with enhanced tuning switch-less tertiary winding and 208.8 dBc/Hz peak FoMT in 22 nm FDSOI," in *Proc. IEEE Radio Freq. Integr. Circuits Symp. (RFIC)*, Aug. 2020, pp. 247–250.
- [37] M. A. Hoque, M. Chahardori, P. Agarwal, M. A. Mokri, and D. Heo, "Octave frequency range triple-band low phase noise K/Ka-band VCO with a new dual-path inductor," in *IEEE MTT-S Int. Microw. Symp. Dig.*, Aug. 2020, pp. 341–344.
- [38] Y. Shu, H. J. Qian, and X. Luo, "A 18.6-to-40.1 GHz 201.7 dBc/Hz FoMT multi-core oscillator using E-M mixed-coupling resonance boosting," in *IEEE Int. Solid-State Circuits Conf. (ISSCC) Dig. Tech. Papers*, Feb. 2020, pp. 272–274.
- [39] H. Jia, W. Deng, P. Guan, Z. Wang, and B. Chi, "A 60 GHz 186.5 dBc/Hz FoM quad-core fundamental VCO using circular triple-coupled transformer with no mode ambiguity in 65 nm CMOS," in *IEEE Int. Solid-State Circuits Conf. (ISSCC) Dig. Tech. Papers*, Feb. 2021, pp. 1–3.



**Seongwoog Oh** (Graduate Student Member, IEEE) received the B.S. degree in electrical engineering and computer science from the Gwangju Institute of Science and Technology College, Gwangju, South Korea, in 2016, and the M.S. degree in electrical engineering from Seoul National University, Seoul, South Korea, in 2018, where he is currently pursuing the Ph.D. degree in electrical engineering.

His current research interests include the design of microwave integrated circuits, antenna-on-package systems for 5G/6G communication, and microwave brain stimulation.



**Jungsuek Oh** (Senior Member, IEEE) received the B.S. and M.S. degrees from Seoul National University, Seoul, South Korea, in 2002 and 2007, respectively, and the Ph.D. degree from the University of Michigan, Ann Arbor, MI, USA, in 2012.

From 2007 to 2008, he was with Korea Telecom, Seongnam-si, South Korea, as a Hardware Research Engineer, where he was worked on the development of flexible RF devices. In 2012, he was a Post-Doctoral Research Fellow with the Radiation Laboratory, University of Michigan.

From 2013 to 2014, he was a Staff RF Engineer with Samsung Research America, Dallas, TX, USA, where he was worked as a Project Leader for the 5G/millimeter-wave antenna system. From 2015 to 2018, he was a Faculty Member with the Department of Electronic Engineering, Inha University, Incheon, South Korea. He is currently an Associate Professor with the School of Electrical and Computer Engineering, Seoul National University. He has authored more than 50 technical articles. His research interests include mmWave/THz beam-focusing/shaping techniques, antenna miniaturization for integrated systems, and radio propagation modeling for indoor scenarios.

Dr. Oh has served as a TPC Member and the Session Chair for the IEEE Antennas and Propagation Society (AP-S)/US National Committee (USNC)-International Union of Radio Science (URSI) and International Symposium on Antennas and Propagation (ISAP). He was a recipient of the 2011 Rackham Predoctoral Fellowship Award at the University of Michigan, the 2018 SNU Creative-Pioneering Research Award, and the 2019 IEEE AP-S/MTT Seoul Chapter Best Paper Award. He has been an Associate Editor of *Microwave and Optical Technology Letters* and *ICT Express*.